Kinetic Study of a Direct Water Synthesis over Silica-Supported Gold Nanoparticles[†]

David G. Barton* and Simon G. Podkolzin

The Dow Chemical Company, Core Research, Midland, Michigan 48674

Received: March 15, 2004; In Final Form: August 8, 2004

The reaction mechanism of water formation from H_2 and O_2 was studied over a series of silica-supported gold nanoparticles. The metal particle size distributions were estimated with TEM and XRD measurements. Hydrogen and oxygen adsorption calorimetry was used to probe the nature and properties of surface species formed by these molecules. DFT calculations with Au_5, Au_{13}, and Au_{55} clusters and with Au(111) and Au(211) periodic slabs were performed to estimate the thermodynamic stability and reactivity of surface species. Kinetic measurements were performed by varying the reactant partial pressures at 433 K and by varying the temperature from 383 to 483 K at 2.5 kPa of O_2 and 5 kPa of H_2. The measured apparent power law kinetic parameters were similar for all catalysts in this study: hydrogen order of 0.7–0.8, oxygen order of 0.1–0.2, and activation energy of 37–41 kJ/mol. Catalysts with Si–MFI (Silicalite-1) and Ti–MFI (TS-1 with 1 wt % Ti) exhibited similar activities. The activities of these catalysts with the MFI crystalline supports were 60–70 times higher than that of an analogous catalyst with an amorphous silica support. Water addition in the inlet stream at 3 vol % did not affect the reaction rates. The mechanism of water formation over gold is proposed to proceed through the formation of OOH and H_2O_2 intermediates. A rate expression derived based on this mechanism accurately describes the experimental kinetic data. The higher activity of the MFI-supported catalysts is attributed to a higher concentration of gold particles comparable in size to Au_{13}, which can fit inside MFI pores. DFT results suggest that such intermediate-size gold particles are most reactive toward water formation. Smaller particles are proposed to be less reactive due to the instability of the OOH intermediate whereas larger particles are less reactive due to the instability of adsorbed oxygen.

1. Introduction

A kinetic evaluation of hydrogen oxidation over gold was first reported nearly a century ago by Bone and Wheeler, in what was one of the first systematic studies of the dependence of reaction rates on reactant gas pressures.[1] These authors used 53 g of gold gauze at 523 K in a recirculation reactor system to evaluate the kinetic reaction orders. Their work was critiqued and extended 20 years later by Benton and Elgin who conducted kinetic experiments in a flow through system with a gold nugget at 403 K.[2] Although the reaction mechanism over solid gold catalysts was investigated in later studies (for example, Ostrovskii and Dobrovol'skii reported reaction rates as a function of oxygen surface coverage[3]) mechanism details still remain largely unknown. This mechanism is likely to involve different steps than the well-studied reactions of H_2 and O_2 on surfaces of Pt, Pd, and other noble metals where these molecules readily adsorb and dissociate at ambient conditions.

Recent studies of H_2 and O_2 reactions over gold focused on properties of supported gold nanoparticles, especially on the formation and stability of H_2O_2 on these particles. Specifically, Jones and Grey patented a process for H_2O_2 production using a supported gold catalyst.[4] Landon et al. studied H_2O_2 formation over gold particles supported on Al_2O_3 and ZnO and Okumera et al. on SiO_2, MCM-41, and active carbon.[5,6] Lunsford et al. reported on the stability of OH radicals on gold nanoparticles supported on TiO_2, SiO_2, and Al_2O_3 and suggested that OH decomposition proceeds through H_2O_2 formation via coupling reactions.[7]

The nature of the catalytic activity of gold nanoparticles for CO oxidation, low-temperature water-gas shift, and hydrogenation reactions has been actively studied recently. Current hypotheses for catalytic activity of gold nanoparticles have been summarized by Cho.[8] These hypotheses include effects of the gold particle size, particle geometry, and the gold–support interaction. Studied reactions have been shown to be strongly structure sensitive: influenced by the size and texture of gold nanoparticles. The geometries of nanoparticles, in turn, depend on the gold interaction with the catalyst support, catalyst preparation methods, and pretreatment conditions.

The effect of the gold particle size for hydrogen oxidation over silica-supported gold nanoparticles was studied by Naito and Tanimoto.[9] They observed that large gold particles (0.1–5 wt % Au/SiO$_2$) primarily catalyzed H_2O formation, and, in contrast, small gold particles (0.05 and lower wt % Au/SiO$_2$) primarily catalyzed the H–D exchange reaction. The current study attempts to elucidate the reaction mechanism of H_2O formation and its dependency on the size of gold nanoparticles by measuring kinetic rates over similar catalysts: 5 and 0.15 wt % Au/SiO$_2$. Furthermore, these catalysts on an amorphous silica support are compared to gold nanoparticles on crystalline supports with the MFI structure. The size of the cavity at the intersection of the pores, which are ~5.5 Å in the MFI structure, puts a restriction on the maximum size of gold particles inside the MFI structure. Catalysts were prepared with a gold loading of 0.15 wt % using two types of MFI supports: Si–MFI (Silicalite-1) and Ti–MFI (TS-1) (Table 1). The effect of the support crystallinity and pore-size restrictions was evaluated by comparing an amorphous SiO_2 support with a Si–MFI support. The effect of the gold–support interaction was evaluated by

---

* To whom correspondence should be addressed: DGBarton@dow.com.

Water Synthesis over Gold Nanoparticles

J. Phys. Chem. B, Vol. 109, No. 6, 2005 **2263**

TABLE 1: Adsorption Calorimetry Results Showing Coverage Values for O_2 Titration with Subsequent Evacuation and Back-Titration with H_2 at 400 K, μmol/g

catalyst	θ of O_2 strongly bound based on heat evolution	θ of H_2 based on heat evolution	θ of H_2 saturation	θ of H_2/ θ of O_2	θ of H_2 sat/ θ of O_2
5 wt % Au on SiO_2	0.40	0.38	0.64	1.0	1.7
0.15 wt % Au on SiO_2	0.16	0.18	0.38	1.1	2.1
0.15 wt % Au on Si−MFI	0.17	0.21	0.45	1.2	2.1
0.15 wt % Au on Ti−MFI	0.22	0.24	0.52	1.1	2.2
0.15 wt % Au on Si−MFI after high *T* treatment	0.21	0.21	0.37	1.0	1.8

comparing catalysts with Si−MFI and Ti−MFI supports. One additional catalyst sample was prepared by exposing the original 0.15 wt % Au/Si−MFI catalyst to a high-temperature pretreatment in the presence of H_2 and O_2 in an attempt to accelerate aging. This aged sample was intended to provide information on the stability of gold nanoparticles and on the direction of any changes in their properties with time on stream.

Kinetic measurements for the rate of H_2O formation from H_2 and O_2 in He were conducted by varying the reactant partial pressures at 433 K and by varying the temperature from 383 to 483 K at 2.5 kPa of O_2 and 5 kPa of H_2. The kinetic experiments were repeated with 3 kPa of H_2O in the inlet stream to investigate the extent of product inhibition. The size of gold nanoparticles was estimated with transmission electron microscopy (TEM) and X-ray diffraction (XRD). The catalysts were additionally characterized by O_2 and H_2 adsorption calorimetry. Density functional theory (DFT) calculations for models representing gold particles of different sizes were used to estimate energetics of surface reactions and analyze possible reaction schemes. The computational results were used to identify energetic trends as a function of the gold particle size. The catalyst characterization data and computational results were consolidated into a reaction mechanism that accurately described the collected kinetic data.

2. Experimental Section

a. Catalyst Preparation. Gold catalysts were prepared with three supports: Saint-Gobain Norpro amorphous SiO_2 (Norton XS 16080, 120 m²/g), Si−MFI (Silicate-1), and Ti−MFI (TS-1, MFI structure with 1.0 wt % Ti)[10] with a standard loading of 0.15 wt % Au on each support and one with a 5 wt % Au loading on Saint-Gobain Norpro SiO_2. Samples were prepared by an aqueous incipient wetness impregnation using an $HAuCl_4$ (Aldrich, ACS Reagent) and sodium acetate (Aldrich, 99.99%, ReagentPlus) solution to give the desired loading of Au and the atomic ratio of Na/Au of 22/1. The effect of Na and Cl presence was not considered in the current study because it was expected to be minor compared to the gold particle size effect based on multiple published CO oxidation studies recently summarized by Nørskov et al.[11] The samples were dried in a vacuum at 343 K for 2 h. The Au loadings and amount of Ti in Ti−MFI were confirmed with elemental analysis. The MFI structure was confirmed with XRD, and the Ti coordination in Ti−MFI was confirmed with UV−vis spectroscopy.

An additional Si−MFI-supported catalyst was prepared by pretreating the original 0.15 wt % Au/Si−MFI sample at high temperature in water vapor. This pretreatment was done by exposing the sample to 5 kPa of H_2 and 2.5 kPa of O_2 in He at 600 K with the total flow rate of 120 sccm for 15 h. Under these conditions, a complete conversion of the reactants into water was observed.

b. TEM and XRD. High-resolution transmission electron micrographs (TEM) were recorded with a JEOL 2010F instrument, which used a field emission gun (FEG) with an accelerat-

ing voltage of 200 keV. Conventional TEM images were captured with a Gatan multiscan MSC794 digital camera. High-angle annular dark field (HAADF) images were obtained using the scanning TEM (STEM) unit attached to the JEOL 2010F. The dark field images were produced by scanning a fine probe (~2.5 Å in diameter) across the sample and collecting the electrons that were scattered onto an annular detector. The STEM images were recorded using Gatan Digital Micrograph/Digiscan software with a 512 × 512 pixel area and 60 s acquisition time.

X-ray diffraction (XRD) data were collected with a Bruker D4 Endeavor system equipped with an active Si(Li) solid-state Sol-X detector. A Cu-filament tube (1.5418 λ) with a power level of 1.6 kW (40 kV, 40 mA) was used, with the antiscatter and detector slits being set to 1 mm and the step size to 0.01°.

c. Calorimetry. Microcalorimetric measurements were collected with a Setaram BT2.15D calorimeter, using the same equipment and techniques as in experiments with Pt−Au/SiO_2 samples reported earlier.[12] The employed methodology of O_2 titration followed by H_2 back-titration, pioneered by Boudart for Pt and Pd,[13−15] follows the method used recently for Au/Al_2O_3.[16] Pretreatment and titration conditions were selected in such a way as to estimate the fraction of sites that are likely to adsorb O_2 under the reaction conditions in the kinetic experiments, as opposed to alternative conditions which could be used to estimate the fraction of exposed metal atoms.

Samples (0.8−1.1 g) previously activated in H_2 and O_2 flow in the kinetic reactor were pretreated initially with H_2 (99.999%, AGA Inc., flow rate of 300 sccm) by raising the temperature to 473 K in 1 h and then holding at this temperature for 2 h. The samples were then purged with He (99.999%, AGA Inc., flow rate of 300 sccm) at 473 K for 1 h and torch sealed in the sidearm of the pretreatment Pyrex cell, producing a Pyrex capsule with the catalyst under He. The catalyst capsule was subsequently broken inside a set of calorimetric cells immediately before conducting adsorption measurements.

Titration with O_2 (99.99%, 0.5 ppm of CO, 1 ppm of H_2, less than 0.5 ppm hydrocarbons, AGA Inc.) was performed first to the residual pressure of ~1 kPa. Then, gas-phase O_2 was evacuated at a dynamic pressure of 10^{-3} Pa at the experimental temperature of 400 K for 1 h. The remaining adsorbed oxygen was back-titrated with H_2 (99.999%, AGA Inc.) at the same temperature. The gases used for the titration were additionally purified by passing over a bed of copper turnings at 673 K and molecular sieves at 77 K. Volumetric and calorimetric data were collected by introducing small, 1−10 μmol, gas doses and monitoring the residual pressure and heat response. The heat response was recorded as a function of time and integrated to determine the energy released during each dose. The differential enthalpies of adsorption, ΔH_{ads}, were calculated for each dose by dividing the heat released by the amount of the gas adsorbed. The equilibration and data collection time was 15−30 min for each dose. The volumetric system had a dynamic vacuum of about 1 × 10^{-5} Pa, and the maximum apparent leak rate was
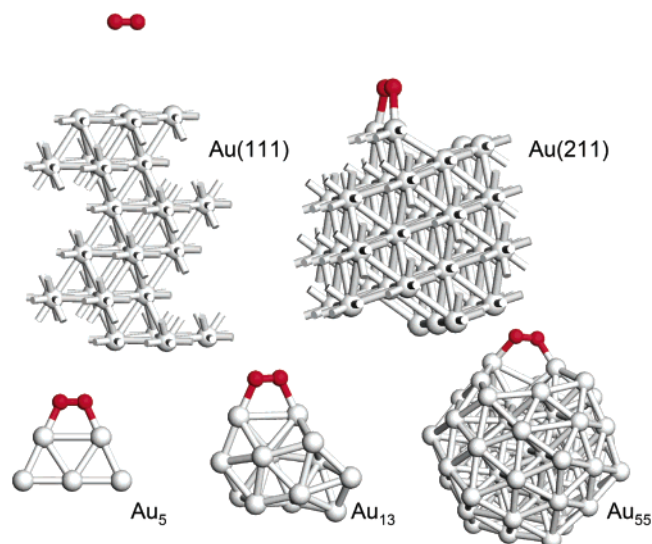
**Figure 1.** Computational models of gold surfaces. Models are shown with optimized O_2 geometries. For Au(111) and Au(211), a single unit cell of the periodic slab is shown.

on the order of 10^{-6} μmol/min. Adsorption measurements are reported as the amount of gas adsorbed per total catalyst weight (μmol/g).

d. Computational Methods. Gradient-corrected spin polarized periodic density functional theory (DFT) calculations were performed using the DMol3 code in Materials Studio 2.2 software by Accelrys Inc. The calculations used the double numerical with polarization (DNP) basis set and the generalized gradient-corrected Perdew, Burke, and Enzerhof (GGA PBE 1996) functional. Tightly bound core electrons were represented with semicore pseudopotentials. The calculated equilibrium Au lattice constant of 4.197 Å closely matched the accepted experimental value of 4.078 Å.

A number of model gold surfaces were constructed for evaluating the effect of the metal particle size on the stability of oxygen- and hydrogen-derived adsorbed species. The considered gold models are shown in Figure 1. Models of small particles were limited to gold clusters with an odd number of atoms because previous theoretical calculations indicate that such clusters bind adsorbates more strongly.[17] The Au_5 cluster with a size similar to that of toluene ($\sim$5 Å) was chosen to represent small metal particles that fit into MFI pores. The optimized structure of Au_5 in Figure 1 is in agreement with the reported computational study on the geometries of small Au particles by Bonacic-Koutecky et al., who showed that clusters with fewer than 12 atoms tend to be flat.[18] The Au_{13} cluster ($\sim$7 Å) was chosen based on the size restriction of the MFI pore intersections. A schematic comparison between the sizes of the model Au_5 and Au_{13} clusters and the 10-ring MFI pore (5.3×5.6 Å in the (010) plane) is shown in Figure 2. The optimized geometry of the Au_{13} cluster in Figure 1 was chosen by evaluating multiple configurations, and it is similar to the previously identified low-energy Au_{13} amorphous structure.[19] The Au_{55} icosahedron ($\sim$11 Å) was selected to represent particles that cannot fit into MFI pores or pore intersections. The initial Au_{55} icosahedron geometry was optimized by adsorbing an oxygen atom and then removing it. Adsorption of additional oxygen atoms (up to eight) in various positions with subsequent removal did not lead to a lower cluster energy. The Au(111) and Au(211) crystal planes were chosen as models of smooth and rough surfaces, respectively, of large metal particles.[20,21] The crystal planes were modeled with infinite slabs,
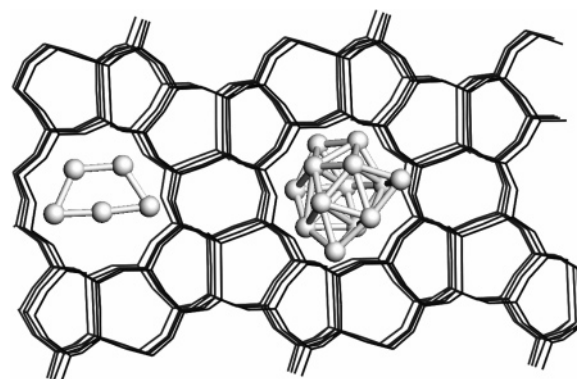
Figure 2. Schematic comparison between MFI pores and model Au clusters: Au_5 fits in the 10-ring pore; Au_{13} may fit in a pore intersection.

constructed as unit cells with periodic boundary conditions. The considered 2×2 unit cells with six layers are presented in Figure 1. The bottom four slab layers were constrained during the calculations, and the top two layers were optimized with an adsorbate, simulating surface relaxation on adsorption. A vacuum spacing of 25 Å was used. Reciprocal-space integration over the Brillouin zone was approximated through k-point sampling with a separation of 0.04 1/Å using the Monkhorst-Pack grid: $5 \times 5 \times 1$ k-points for Au(111) and $3 \times 4 \times 1$ for Au(211).

In addition to evaluating adsorbate energetics, the Au(211) model was used to estimate activation energies by constrained optimization. For all evaluated reactions, with the exception of H_2O_2 decomposition into two OH groups, the H−O distance of a forming or breaking bond was incrementally constrained from the value in the reactant structure to that in the product geometry, while optimizing all other degrees of freedom. For H_2O_2 decomposition into two OH groups, the geometry optimization was performed with the O−O bond being constrained. A transition state estimate was identified as a structure with the maximum energy and with the characteristic transition from a repulsive to an attractive force along the constrained reaction coordinate.

All adsorption, reaction, and activation energies were calculated at 0 K without zero-energy corrections. The usually stated accuracy of DFT calculations for predicting adsorption energies is about 20 kJ/mol. Since this accuracy value depends on the validity of the employed surface models and calculation details, our computational results were interpreted mostly in terms of relative energetic trends as a function of the gold particle size by comparing different models, rather than in terms of absolute values for a single model.

e. Kinetic Measurements. Catalyst samples (0.1−1.0 g) with 0.2−0.5 mm particle sizes were tested in a stainless steel tubular reactor with the internal diameter of 5 mm diluted with an equal volume of 0.2−0.5 mm quartz chips. The size of the catalyst particles and the amount of diluent were varied to ensure the absence of heat and mass transfer limitations. Prior to collecting kinetic data, catalysts were activated first by a temperature treatment in He (99.999%, Ultrahigh Purity grade 5, BOC) flow of 150 sccm at 433 K for 1 h. The catalysts were then pretreated with a mixture of 10 vol % O_2 (99.6% extra dry 2.6 grade, BOC) and 10 vol % H_2 (99.999%, Ultrahigh Purity grade 5, BOC) in He with the total flow rate of 250 sccm at 413 K for 5 h and after that, purged with He only at the same conditions for 1 h.

The inlet and outlet streams were analyzed with a VG Prima 600S magnetic-sector process mass spectrometer. The base

Water Synthesis over Gold Nanoparticles

J. Phys. Chem. B, Vol. 109, No. 6, 2005 **2265**
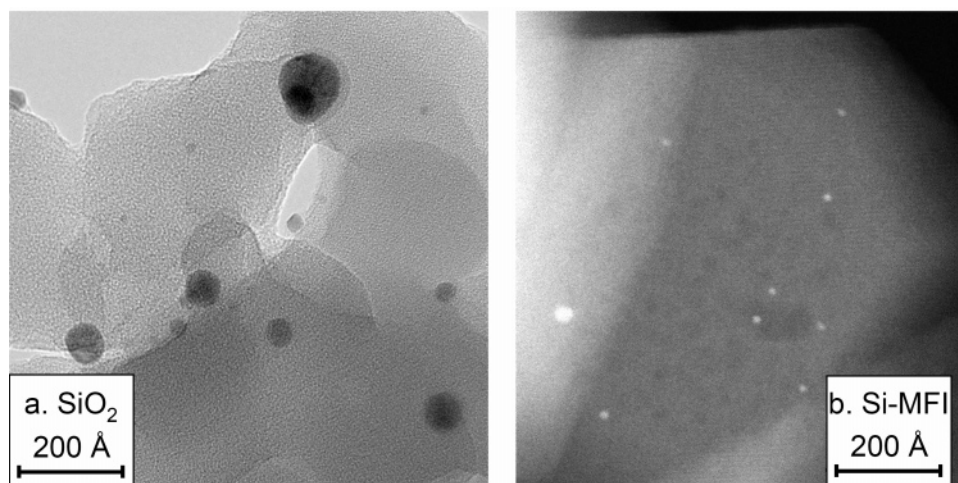
Figure 3. Typical STEM images of supported gold particles: (a) 0.15 wt % Au/SiO$_2$ dark field; (b) 0.15 wt % Au/Si−MFI bright field.
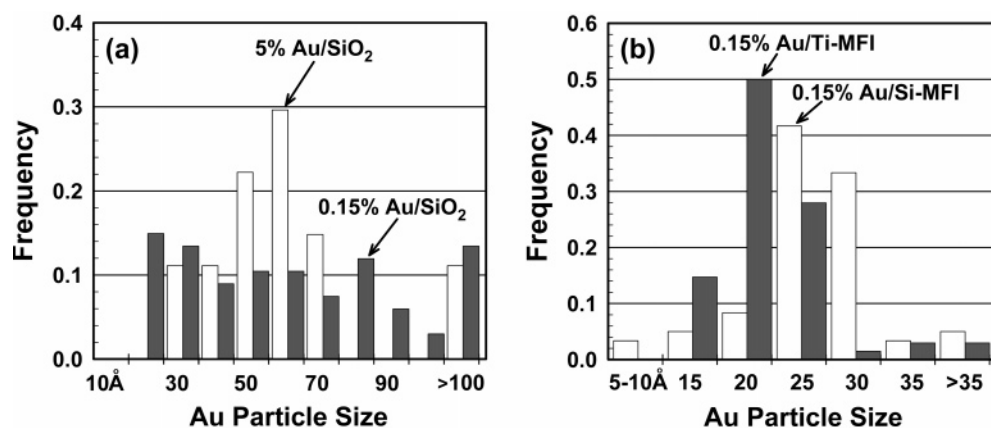
Figure 4. Particle size distributions based on STEM images.

conditions for kinetic testing were 2.5 kPa of O$_2$ and 5 kPa of H$_2$ in He at a total pressure of 101 kPa at 433 K. Under these conditions, a blank experiment was conducted with only support materials (0.333 g each): SiO$_2$, Si−MFI, and Ti−MFI. The reaction rate for the mixture of supports was 30 times lower on catalyst weight basis compared to that of 0.15 wt % Au/SiO$_2$. Data on the dependency of the reaction rate on the reactant partial pressures were collected by varying the feed composition at 433 K. Hydrogen pressure was varied in the range of 0.5− 20 kPa while holding oxygen pressure constant at 2.5 kPa and oxygen pressure was varied in the range of 2−40 kPa while holding hydrogen pressure constant at 5 kPa. Water formation rates are reported as turnover frequencies based on the total amount of gold (TOF, mol H$_2$O (mol of Au·s)$^{-1}$). The activation energy was estimated by varying the temperature from 383 to 483 K at 2.5 kPa of O$_2$ and 5 kPa of H$_2$. The order of experiments was randomized, and in addition, each set of conditions was evaluated at least twice. The catalyst deactivation was monitored by continually retesting at the base conditions of 2.5 kPa of O$_2$ and 5 kPa of H$_2$ at 433 K: data at the base conditions were collected repeatedly after completion of three different sets of conditions from the randomized schedule. The activity data were adjusted using linear interpolation based on the deactivation results.

All kinetic experiments were repeated at the same conditions in the presence of deionized water. Water was introduced by passing a reactant mixture through a saturator at room temperature. The inlet water concentration was continually monitored and found to vary in a narrow range of 2.90−2.97 vol %. For all kinetic measurements, the total flow rate was adjusted to

maintain the conversion of both H$_2$ and O$_2$ below 10% in order to enable the use of a differential reactor model in data analysis.
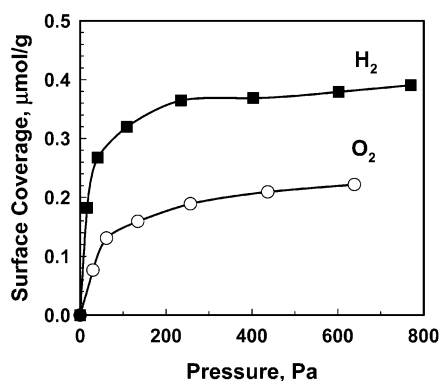
3. Results

a. TEM and XRD. Typical TEM images for amorphous and crystalline supports are shown in Figure 3. Multiple representative images were analyzed to determine histograms of gold particle size distributions illustrated in Figure 4. The particle size detection limit was 5−7 Å. In contrast to amorphous SiO$_2$, a large portion of gold particles on the MFI supports could be located inside the pores, which would have made them undetectable by TEM. The histograms of the metal particles on the outer surface in Figure 4b indicate that most of the detectable Au particles on the MFI supports had the size of 15−30 Å. The histogram for the 0.15 wt % Au/Si−MFI sample after the high temperature pretreatment was essentially the same (not shown in Figures). The gold particles on the 0.15 wt % Au/SiO$_2$ sample had a broad and almost uniform distribution from 20 to greater than 100 Å (Figure 4a). The majority of the particles on the 5 wt % Au/SiO$_2$ were in the size range of 50− 70 Å, with the rest of them being in the ranges of 30−40 Å or greater than 100 Å (Figure 4a).

For the catalysts with 0.15 wt % Au loading, no XRD diffraction lines attributed to gold were detected. The 5 wt % Au/SiO$_2$ sample, in contrast, had a strong gold pattern. An average gold particle size value of 120 Å was estimated based on a line broadening fit. This result is in general agreement with the TEM data in Figure 4a, which show that a significant number of Au particles on this catalyst had the size of greater than 100 Å.

TABLE 2: DFT Estimates for Adsorption Energies of Gas-phase Radicals and Molecules, kJ/mol

Species	Au particle size increases					Sensitivity to particle size[a]
Model surface	Au(111)	Au(211)	Au_{55}	Au_{13}	Au_5	
H_2	-2	-1	-4	-3	-29	27
H	-211	-225	-224	-277	-301	90
O_2	0	-5	-6	-53	-136	136
O	-315	-318	-333	-353	-360	42
H_2O	-18	-25	-19	-29	-32	14
H_2O_2	-20	-24	-20	-25	-28	8
OH	-190	-238	-231	-260	-322	132
OOH	-52	-83	-81	-114	-163	111

[a] Sensitivity to particle size is defined as the difference between the maximum and minimum values predicted for models of different particle sizes.

Figure 5. Typical adsorption isotherms obtained in calorimetric experiments. Initial titration with O_2, followed by evacuation, followed by back-titration with H_2 at 400 K. Shown are results for 0.15 wt % Au/SiO_2.

b. Adsorption Calorimetry. Heat evolution was detected on introduction of 1−3 initial O_2 doses. The initial enthalpy of adsorption was estimated at −150 to −220 kJ/mol. Small uptake and rapid decline of the differential heat of adsorption with increasing coverage made it difficult to estimate the heat of O_2 adsorption more accurately and discriminate the energetics for the different samples. Once the heat of adsorption declined to an undetectable value at an equilibrium pressure of ∼200 Pa, the measured surface coverage for samples with the amorphous SiO_2 approached a saturation value, as can be seen in Figure 5 where a typical O_2 adsorption isotherm is presented. For the MFI-supported samples, however, there was no clear saturation limit. As a result, a comparison of O_2 coverage values was made based on estimates for amounts of strongly bound oxygen, defined as adsorbed O_2 associated with heat evolution. The oxygen coverage estimates are provided in Table 1. All catalysts with 0.15 wt % Au loading had similar O_2 coverage values of 0.16−0.22 μmol/g, which corresponds to 2.1−2.9% coverage based on the total number of gold atoms. The absolute coverage for the high loading 5 wt % Au/SiO_2 sample was ∼2 times higher: 0.40 μmol/g, but as a relative amount of the total number of gold atoms, it was significantly lower: 0.2%. After evacuation of gas-phase O_2 and weakly bound oxygen species, H_2 was used to back-titrate the remaining surface oxygen. Previous adsorption measurements with the same equipment using a 9.78 wt % Au/SiO_2 sample with a CO saturation coverage of ∼1 μmol/g[12] showed that the H_2 uptake at room temperature without preadsorbed O_2 was undetectably small (<0.1 μmol/g), which is in agreement with well-established H_2 adsorption studies with Au films.[22,23] During the H_2 back-titration, the initial heat of adsorption was −120 to −150 kJ/mol. The detected heat declined rapidly with each subsequent dose, and no heat evolution was detected after the initial two to three doses. The estimates for the H_2 coverage values associated with the heat evolution and for the saturation coverage values are shown in Table 1. Also shown in this table are ratios of H_2 and O_2 coverage values. These ratios are similar for all our catalysts, and they suggest that the heat evolution on H_2 introduction is associated with the stoichiometry of H_2O_2, and the saturation H_2 coverage corresponds to the H_2O stoichiometry. The shape of the H_2 adsorption isotherm in Figure 5 suggests that no gas-phase H_2O was produced because each mole of H_2 would have produced a mole of H_2O, and consequently, no H_2 uptake would have been detected based on the residual pressure reduction. For comparison with the H_2 uptake, the saturation CO coverage on a reduced 0.15 wt % Au/Si−MFI sample was measured at room temperature (0.51 μmol/g) and found to be similar to the saturation H_2 coverage of 0.45 μmol/g (Table 1).

c. DFT Results. Only a summary of the DFT results that are essential for the development of a kinetic model are provided in this study. Details of surface model development and optimized adsorbate geometries will be reported separately. The calculated estimates for adsorption energies are provided in Table 2. These adsorption energies suggest a general trend of higher adsorbate stability (lower adsorption energies) on smaller gold clusters. The estimates for Au_{55} and Au(211) are substantially similar, suggesting that Au(211) could be an efficient model for gold particles with about 55 atoms. The stabilization effect with decreasing gold particle size varies significantly for various surface species; and this effect was quantified with a sensitivity parameter, defined as the difference between the maximum and minimum predicted adsorption energy values for each adsorbate (Table 2). Specifically, it was the difference between the adsorption energies for Au(111), where adsorbates were least stable, and those for Au_5, where adsorbates were most stable. The adsorption of molecular oxygen was estimated to have the largest sensitivity; no adsorption was predicted for Au(111), whereas an adsorption energy of −136 kJ/mol was predicted for Au_5, yielding the sensitivity of 136 kJ/mol (Table 2). The sensitivity estimates for OH and OOH radicals were also large: 132 and 111 kJ/mol, respectively, suggesting that the particle size effect is significant for these species. The sensitivity estimates for H and O radicals were lower: 90 and 42 kJ/mol, respectively, suggesting a moderate dependency of their stability on the particle size. And finally, for H_2, H_2O, and H_2O_2, the adsorption energies and sensitivity values were less than 30 kJ/mol, suggesting that these species adsorb weakly, regardless of the particle size.

Water Synthesis over Gold Nanoparticles

J. Phys. Chem. B, Vol. 109, No. 6, 2005 **2267**

TABLE 3: DFT Estimates for Gas-Phase Reaction Energies, kJ/mol[a]

reaction	ΔE
$H_2 = 2\,H$	438
$O_2 = 2\,O$	634
$H_2 + 0.5\,O_2 = H_2O$	−239
$H_2 + O_2 = H_2O_2$	−142
$H_2O = H + OH$	528
$H_2O_2 = 2\,OH$	282
$H_2O_2 = OOH + H$	365

[a] The calculations were performed at the same level of theory as the one used for Au surface calculations.

Results of DFT calculations for gas-phase reactions of H_2 and O_2 at the same level of theory are provided in Table 3. These gas-phase results and the adsorption energies in Table 2 were used to estimate energetics of selected surface reactions in Table 5 by constructing appropriate thermodynamic cycles. Since preferential adsorption sites for each evaluated surface model were similar for all considered adsorbates, a single-site adsorption model was initially considered. For example, the energy change for oxygen-assisted hydrogen dissociation with the formation of a hydrogen peroxide surface species, $O_2^* + H_2$ (gas) + * = OOH* + H* (reaction 8 in Table 5), was estimated for Au₅ as a combination of the following steps: O_2 desorption (136 kJ/mol, Table 2), gas-phase H_2O_2 formation and decomposition (−142+365 kJ/mol, Table 3), and adsorption of the formed OOH and H radicals (−163−301 kJ/mol, Table 2), giving the combined ΔE of −105 kJ/mol. The inherent inaccuracy of such estimates of surface reaction energetics arises from the neglect of coverage effects because the adsorption energies in Table 2 were calculated with a single adsorbate on a cluster or in a unit cell, whereas surface reactions usually involve two or more neighboring adsorbates. Nevertheless, the DFT estimates for reaction energies should still be useful for
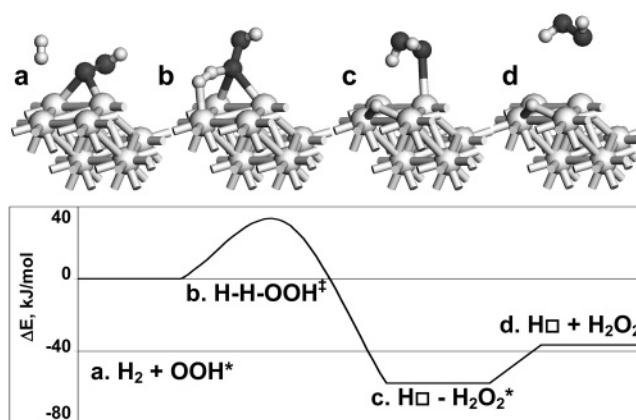
Figure 6. Energy diagram for reaction 4 in Table 6, OOH* + H₂ (gas) + □ = H₂O₂* + H□, and subsequent H₂O₂ desorption. This H₂O₂ formation reaction is proposed to be the rate-determining step in the H₂O formation mechanism. Only the two top layers of the Au(211) model are shown for clarity in this figure and Figures 7-9. Preferential adsorption site is denoted by *; an alternative hydrogen adsorption site is denoted by □.

identification of trends in the analysis of possible reaction mechanisms and for obtaining initial guesses for kinetic model parameters.

Results of transition state calculations with the Au(211) model are summarized in Table 6 and Figures 6−8. Figure 6a shows that gas-phase hydrogen can stabilize near the surface prior to reacting with adsorbed OOH. In the transition state structure, Figure 6b, one atom of the hydrogen molecule forms a bond with OOH, while the other one is already bonded to the surface. In the product structure, Figure 6c, the formed H₂O₂ occupies the edge site, where OOH was initially bonded, and the split off hydrogen atom adsorbs on the slope of the Au(211) step. Additional calculations with the Au(211) model for arrange-

**TABLE 4: Kinetic Data Summary: Apparent Power-Law Parameters with 95% Confidence Intervals**

catalyst	hydrogen order	oxygen order	activation energy, kJ/mol
5 wt % Au on SiO₂	0.82 ± 0.02	0.08 ± 0.01	41.3 ± 1.0
0.15 wt % Au on SiO₂	0.73 ± 0.02	0.12 ± 0.02	38.2 ± 1.2
0.15 wt % Au on Si−MFI	0.69 ± 0.02	0.19 ± 0.01	38.5 ± 1.0
0.15 wt % Au on Ti−MFI	0.76 ± 0.02	0.17 ± 0.02	37.1 ± 1.1
0.15 wt % Au on Si−MFI after high T treatment	0.76 ± 0.06	0.14 ± 0.02	37.7 ± 1.0
apparent values for fitted data	0.77	0.15	39.0

**TABLE 5: Estimated Reaction Energies Based on Values in Tables 2 and 3, kJ/mol**

Reaction / Model surface	Au particle size increases ←					Sensitivity to particle size[a]
	Au(111)	Au(211)	Au₅₅	Au₁₃	Au₅	
Proposed reaction mechanism based on a single-site model						
1. O₂(gas) + * = O₂*	0	-5	-6	-53	-136	136
2. H₂ (gas) + 2* = 2H*	17	-11	-9	-116	-163	180
3. O₂* + H* = OOH* + *	-56	-69	-66	1	59	128
4. OOH* + H₂ (gas) + * = H₂O₂* + H* (RDS)	-106	-93	-89	-115	-93	26
5. H₂O₂* + * = 2OH*	-77	-169	-160	-212	-333	256
6. OH* + H* = H₂O* + *	-146	-91	-93	-20	62	208
7. H₂O* = * + H₂O (gas)	18	25	19	29	32	14
Other considered reactions						
8. O₂* + H₂ (gas) + * = OOH* + H*	-40	-80	-75	-115	-105	75
9. O₂* + H₂ (gas) = H₂O₂*	-162	-161	-156	-114	-34	128
10. OH* + H₂ (gas) + * = H₂O* + H*	-125	-99	-93	-131	-43	87
11. O₂* + H₂O* = OOH* + OH*	90	22	26	22	-3	93
12. H₂O₂* + * = OOH* + H*	122	82	80	-1	-70	192

[a] Sensitivity to particle size is defined as the difference between the maximum and minimum values predicted for models of different particle sizes.
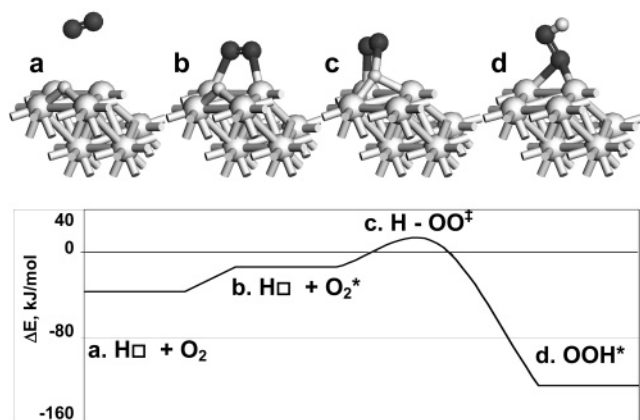
Figure 7. Energy diagram for O_2 adsorption and reaction 3 in Table 6, $O_2^* + H\square = OOH^* + \square$, on Au(211). The combination of this diagram and the diagram in Figure 6 constitutes a catalytic cycle for H_2O_2 formation where H_2 dissociation is assisted by the surface OOH species.
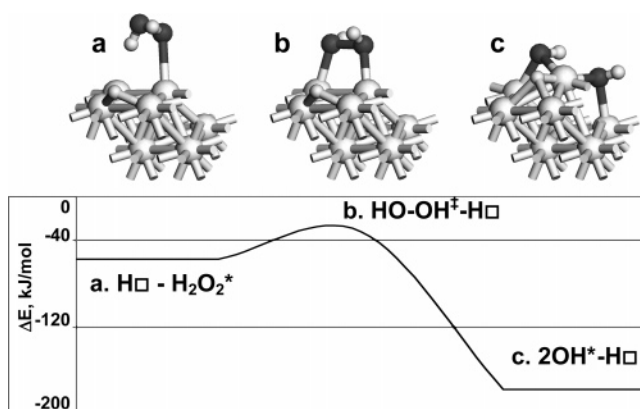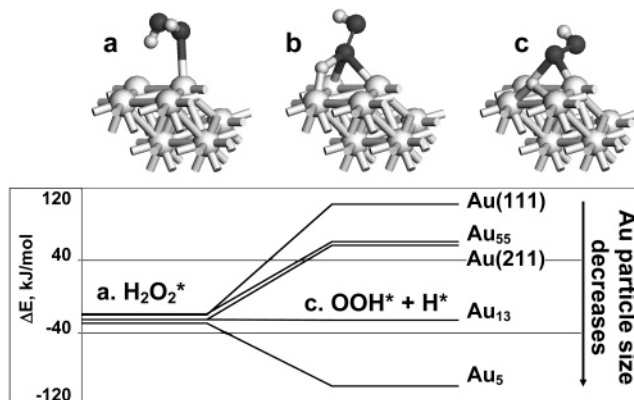

Figure 8. Continuation of the energy diagram in Figure 6c for H_2O_2 decomposition to 2 OH groups in the presence of surface hydrogen, $H_2O_2^* + ^* = 2OH^*$, on Au(211). This reaction is predicted to be more facile than H_2O_2 formation.

TABLE 6: DFT Estimates for Activation Energies on Au(211), kJ/mol[a]

reaction	E_a
1. $OOH^* + H_2 (gas) + \square = H_2O_2^* + H\square$	32
2. $OOH^* + H\square = H_2O_2^* + \square$	30
3. $O_2^* + H_2 (gas) + \square = OOH^* + H\square$	10
4. $O_2^* + H\square = OOH^* + \square$	22
5. $H_2O_2^* + ^* = 2OH^*$	25

a Key: (∗) denotes an adsorption site for all surface species; (□) denotes an additional adsorption site for hydrogen atoms only.

ments where a hydrogen atom adsorbs in the presence of a neighboring H_2O_2, OOH, or O_2 surface species indicate that there are multiple energetically equivalent adsorption sites for the proton. Importantly, a hydrogen atom can adsorb on sites other than the coordinatively unsaturated Au(211) edge site required for oxygen adsorption (Figure 1). A hydrogen atom is stable on those additional sites even when it is the only surface species in the unit cell, as illustrated in Figure 6d; its binding energy, however, is lower by 27 kJ/mol compared to that on the preferred site on the clean surface, which is the same edge bridge site identified for oxygen adsorption in Figure 1. The OOH species are also stable on the additional sites but with the binding energy that is lower by about 40 kJ/mol compared to that for the preferential edge site. Therefore, Au(211) slope sites can be characterized as mostly additional sites for H adsorption. To distinguish the energetic estimates obtained when a hydrogen
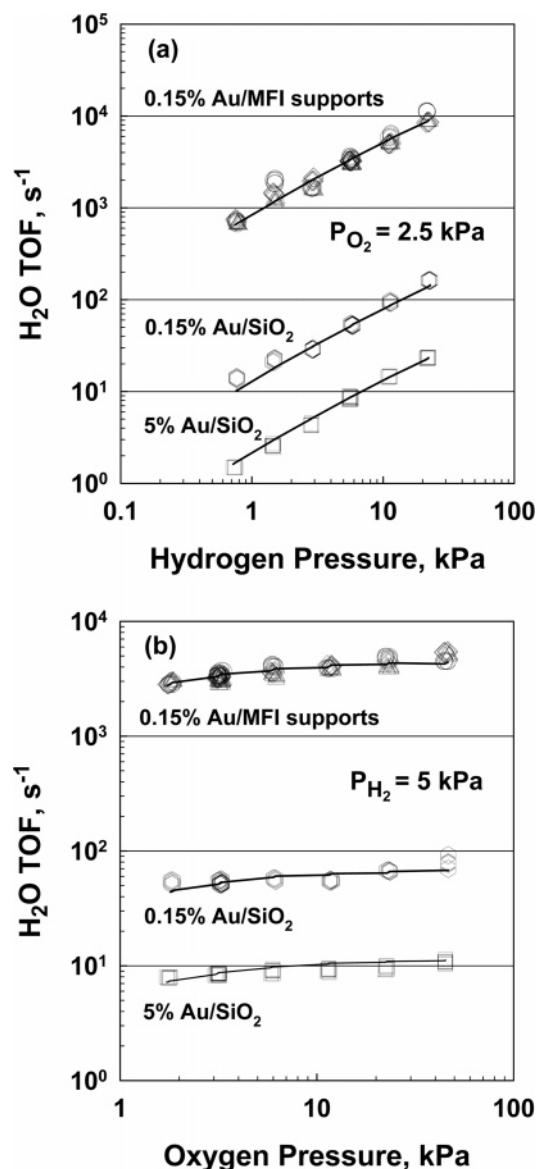
atom adsorbs in proximity to an oxygen-containing species (Table 6 and Figures 6−8) from the reaction energies in Table 5, which were calculated based on hydrogen adsorption on clean surfaces, the alternative hydrogen adsorption site is denoted in Table 6 by a different symbol (□).

The formed H_2O_2 on the surface can (1) desorb or decompose by (2) breaking the O−O bond or by (3) splitting off a hydrogen atom. Figure 7 depicts a continuation of the energy diagram in Figure 6 for the first case, when H_2O_2 desorbs from the active site and O_2 adsorbs in its place. Oxygen adsorption in the presence of adsorbed hydrogen is predicted to be endothermic, Figure 7b, due to the lateral repulsion between the adsorbates. Since oxygen adsorption is estimated to be progressively less favorable on larger gold particles (Table 2), gold particles with the size on the order of Au_{55} and larger are likely to be relatively unreactive toward water formation because of their inability to stabilize adsorbed oxygen. The estimated barrier for the reaction between adsorbed H and O_2 on Au(211) is 22 kJ/mol, Figure 7c and reaction 4 in Table 6. The combination of the energy diagrams in Figures 6 and 7 constitutes a catalytic cycle for H_2O_2 formation where hydrogen dissociation is assisted by the surface OOH species. Initially, when O_2 and H_2 begin to react over a clean catalyst, the surface concentrations of OOH and H species can build up through the reaction of adsorbed O_2 and gas-phase H_2 (reaction 3 in Table 6). This mechanism is similar to the recently proposed H_2O_2 formation mechanism from H_2 and O_2 over an Au_3 cluster.[24] Figure 8 illustrates a continuation of the energy diagram in Figure 6 for the second case, the H_2O_2 decomposition with a breaking of the O−O bond. The estimated barrier for this step is 25 kJ/mol, Figure 8b and reaction 5 in Table 6. This barrier is lower on the energy diagram than the activation energy for H_2O_2 formation in Figure 6b. This relative difference in the stability of the transition states suggests that once formed, H_2O_2 would readily decompose on the Au(211) surface to hydroxyl groups, leading to further reaction with hydrogen and water formation.

The third scenario, the H_2O_2 decomposition with the formation of OOH and H, is analyzed as a function of the gold particle size in Figure 9. This figure visualizes the data for reaction 12 in Table 5 and provides illustrations based on calculations with the Au(211) model (reaction 2 in Table 6). The adsorption energy for H_2O_2 is similar for all the evaluated gold surface models (Table 2). In contrast, OOH and H surface species are predicted to be progressively more stable on smaller gold particles. As a result, the H_2O_2 decomposition with a splitting

Figure 9. Visualization of the relative stability of adsorbed (a) H_2O_2 and (c) OOH and H, reaction 12 in Table 5. The reference state is gas-phase H_2O_2 and a clean Au surface. H_2O_2 decomposition by splitting off H is progressively more thermodynamically favorable on smaller gold particles. Models at the top illustrate (a) the reactant, (b) transition state, and (c) product structures on Au(211), reaction 2 in Table 6.

Water Synthesis over Gold Nanoparticles

J. Phys. Chem. B, Vol. 109, No. 6, 2005 **2269**

Figure 10. Rate of H_2O formation based on the total number of Au atoms at 433 K as a function of (a) H_2 partial pressure, (b) O_2 partial pressure on (□) 5 wt % Au/SiO_2, (○) 0.15 wt % Au/SiO_2, (◇) 0.15 wt % Au/Si−MFI, (△) 0.15 wt % Au/Ti−MFI, and (○) 0.15 wt % Au/Si−MFI-aged with lines showing a fit with dual-site rate expression (eq 2). Rate of H_2O formation was calculated based on the total number of Au atoms.

off of a hydrogen atom is estimated to be progressively less endothermic on Au(111), Au_{55}, and Au(211) and to be thermoneutral on Au_{13} and exothermic on Au_5· H_2O_2 is estimated to be more thermodynamically stable than surface OOH and H on Au_{55} by about 80 kJ/mol, which is significantly higher than any estimated reaction barrier in Table 6. This suggests that H_2O_2 on Au_{55} and larger gold particles is much more likely to decompose by breaking the O−O bond, leading to water formation. On the other hand, OOH and H are more thermodynamically stable than H_2O_2 on Au_5 by about 60 kJ/mol, which is again higher than the estimated reaction barriers in Table 6. H_2O_2 can still form on small gold particles through reaction 1 in Table 6 because this reaction of OOH with gas-phase H_2 is predicted to be exothermic for all gold surfaces due to the stabilization of one of the H_2 atoms on the surface. However, the OOH species are likely to be transient on Au_5 because they are estimated to be less stable compared to surface O_2 and H by 59 kJ/mol (reaction 3 in Table 5). Similarly, water adsorbed
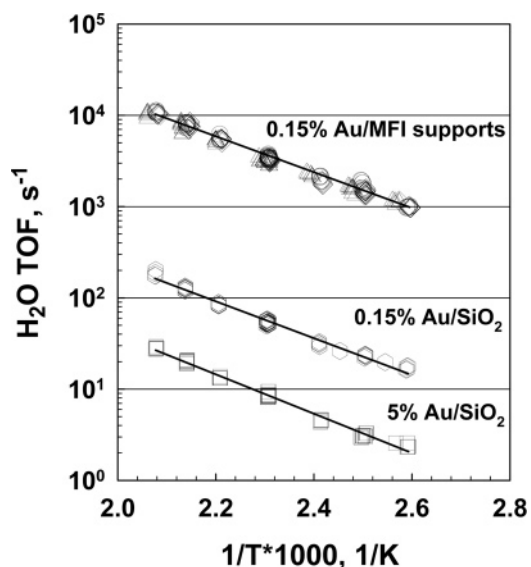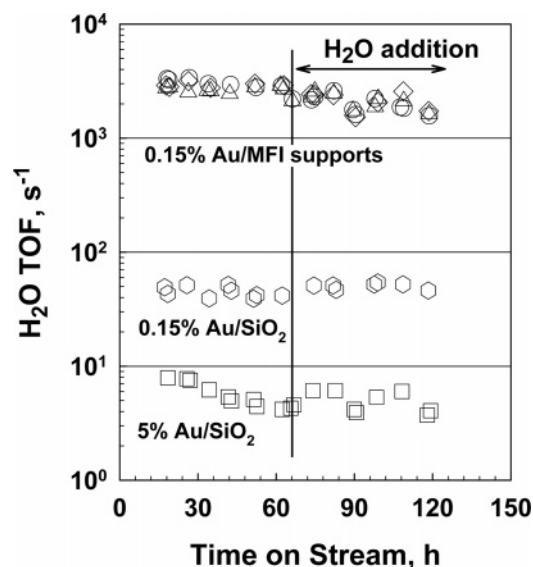

Figure 11. Arrhenius plot at 2.5 kPa of O_2 and 5 kPa of H_2 for (□) 5 wt % Au/SiO_2, (○) 0.15 wt % Au/SiO_2, (◇) 0.15 wt % Au/Si−MFI, (△) 0.15 wt % Au/Ti−MFI, and (○) 0.15 wt % Au/Si−MFI-aged with lines showing a fit with the rate expression based on the dual-site adsorption mechanism (eq 2). Rate of H_2O formation was calculated based on the total number of Au atoms.

on Au_5 is estimated to be less stable than surface OH and H by 62 kJ/mol (reaction 6 in Table 5). These results suggest that O_2 and H species would be a thermodynamic sink on small gold particle, and that such particles are likely to catalyze mostly hydrogen dissociation on the surface assisted by adsorbed oxygen.

d. Reaction Kinetics. The dependency of the reaction rate on H_2 partial pressure is presented in Figure 10a and a similar plot for O_2 pressure is presented in Figure 10b. The data appear to be nearly linear on these log−log plots with similar slopes for all catalysts. The simple power law apparent reaction orders ($r_{H_2O} = kP_{O_2}^{\alpha} P_{H_2}^{\beta}$) are summarized in Table 4. The orders in H_2 pressure for 0.5−20 kPa at 2.5 kPa of O_2 are all below unity: 0.7−0.8. The orders in O_2 pressure for 2−40 kPa at 5 kPa of H_2 are close to zero: 0.1−0.2. An Arrhenius plot for the temperature range of 383−483 K at 2.5 kPa of O_2 and 5 kPa of H_2 is provided in Figure 11. The rate data in the Arrhenius plot also appear to be linear with similar slopes for all catalysts. Consequently, the apparent activation energies, summarized in Table 4, are also similar (37−41 kJ/mol). The 5 wt % Au/SiO_2 sample exhibited the lowest absolute activity based on the total number of Au atoms. The activity of the 0.15 wt % Au/SiO_2 sample was 6 times higher, and the activities of the MFI-supported samples were all similar and significantly, 360−400 times, higher (Figure 11).

The catalyst stability data are presented in Figure 12. The activity of the MFI-supported materials declined by ~15% during the first part of the experiment (66 h). The 0.15 wt % Au/SiO_2 catalyst appeared to be stable. In contrast, the 5 wt % Au/SiO_2 catalyst lost about 40% of its initial activity during the same first part of the experiment. In the second part, after 66 h, water was introduced in the inlet stream at ~3 vol %. The data in Figure 12 show that the water introduction did not affect the reaction rates. Furthermore, the presence of water in the inlet stream did not change, within the experimental accuracy, the apparent activation energies or the apparent reaction orders in H_2 and O_2. They were all analogous to those in Table 4.

Figure 12. Stability data and effect of water addition at the base testing conditions of 2.5 kPa of O_2 and 5 kPa of H_2 at 433 K for (□) 5 wt % Au/SiO₂, (○) 0.15 wt % Au/SiO₂, (◇) 0.15 wt % Au/Si−MFI, (△) 0.15 wt % Au/Ti−MFI, and (○) 0.15 wt % Au/Si−MFI-aged. Rate of H_2O formation was calculated based on the total number of Au atoms.

4. Discussion

Reactions between O_2 and H_2 leading to H_2O_2 and H_2O formation on Pt, Pd, Ag, and Au surfaces were evaluated previously theoretically by Sellers et al. with the bond order conservation−Morse potential (BOC−MP) approach.[25] These authors considered a common mechanism for all evaluated metals with O_2 and H_2 surface dissociation and concluded that H_2O_2 formation, in contrast to H_2O formation, would be favored on Au and Ag surfaces because of the relative stability of OH and OOH surface species. Our DFT calculations presented in Table 2 suggest that the difference between the adsorption energy for OH and that for OOH species is similar for gold particles of various sizes. Since the results of Naito and Tanimoto[9] indicate that the rate of water formation depends strongly on the size of gold particles, a different explanation for catalytic activity was considered. Our proposed reaction mechanism, discussed below, does not assume O_2 dissociation and explains activity differences between large and small gold particles based on the stability of OOH and O_2 surface species.

As most of the recent theoretical studies with Au surfaces focused on CO oxidation, we provide a comparison between our results and previously published results for O_2 and O adsorption energies. Our calculations suggest that O_2 does not bind to Au(111), which is in agreement with results of Mavrikakis et al.[20] A small value of 9 kJ/mol was predicted for the same interaction by Mills et al.[17] For O_2 on Au(211), our estimate of −5 kJ/mol (Table 2) agrees well with −12 kJ/mol obtained by Mavrikakis et al.[20] For O_2 on Au₅, our estimate of −136 kJ/mol is lower than −108 kJ/mol reported by Mills et al.[17] This discrepancy is probably due to the difference in the employed functionals. Liu et al. suggested[21] that the PBE functional, used in the current study, gives somewhat improved energetics compared to the PW91 functional employed by Mills et al. Our values for O adsorption on Au(111) and Au(211), −315 and −318 kJ/mol, respectively, are lower than the values of −247 and −308 kJ/mol obtained by Liu et al. with the same PBE functional probably because our model slabs had a larger number of total layers with two relaxing layers instead of one.

Our calorimetric results indicate that the O_2 adsorption enthalpy is on the order of −150 to −220 kJ/mol, which is

lower than the DFT estimates in Table 2 for all considered Au models. The trend for the O_2 adsorption energy in Table 2, however, suggests that oxygen adsorbs more strongly on smaller gold particles. Therefore, it is possible that gold models with more coordinatively unsaturated sites than those considered in this study would be able to predict adsorption energies more in line with the experimental values. Furthermore, gold−support interactions, which were not evaluated computationally in the current study because they have been reported to be less significant compared to the particle size effect,[11] can provide additional adsorbate stabilization due to the combination of the metal−insulator transition, charge transfer, and geometric strain effects. Berndt et al. provided some evidence for the presence of strongly bound oxygen on Au/Al₂O₃ based on their observation that O_2 titration coverage could be increased by performing pretreatment reduction at 673 K instead of 473−523 K.[16] These authors hypothesized that strongly bound oxygen could be located in Au subsurface, similar to what had been reported for Ag. The same explanation was proposed by Choi et al. for O_2 evolution above 600 K in their TPD experiments with Au/SiO₂. The results of our H_2 back-titration measurements, however, suggest that the strongly bound oxygen is associated with the surface metal layer, in agreement with the assignment of Chesters and Somorjai for the O_2 TPD peak at 1173 K in their experiments with Au(111).[26] In summary, our DFT and titration results suggest that strongly bound oxygen can be attributed to adsorbed species on small Au particles. This assumption is used in the analysis of adsorption and kinetic measurements below.

The coverage values for strongly bound oxygen, which were estimated based on calorimetric titration, are similar for all considered catalysts, as shown in Table 1. These values vary from 0.16 to 0.22 μmol/g for 0.15 wt % Au catalysts, and the coverage is about twice as high for the 5 wt % Au sample. There is no apparent correlation between the amount of the strongly bound oxygen and the significantly different water formation rates for the evaluated catalysts. In addition, H_2 adsorption isotherms indicate that no gas-phase water was produced in the titration experiments. Furthermore, DFT estimates for the H_2O adsorption energies in Table 2, which are no less than −32 kJ/mol for all models, indicate that any formed water would have desorbed readily from gold surfaces. Therefore, it is unlikely that water was formed at all in our titration experiments. This conclusion is consistent with the observation of a strong dependence of the H_2O formation rate on the oxygen surface coverage reported by Ostrovskii and Dobrovol'skii.[3] These authors reported that the water formation rate decreased 10-fold when the oxygen surface coverage was decreased by a small fraction on porous unsupported gold at 393 K, suggesting that the remaining strongly bound oxygen did not contribute to a large extent to the overall reaction rate. We, therefore, conclude that strongly bound oxygen adsorbed on small gold particles in our experiments is largely unreactive toward water formation. This conclusion is supported by the results of Naito and Tanimoto who observed that large gold particles (0.1−5 wt % Au/SiO₂) primarily catalyzed H_2O formation, and, in contrast, small gold particles (0.05 and lower wt % Au/SiO₂) primarily catalyzed the H−D exchange reaction at 423 K.[9]

Naito and Tanimoto also reported that they did not observe ¹⁶O₂−¹⁸O₂ exchange during water formation and oxygen-assisted hydrogen dissociation over their catalysts. In addition, Kislyuk and Tret′yakov estimated the activation energy for O_2 dissociation over a gold filament at 1100−1200 K at 57 kJ/mol,[27] which is higher than our apparent activation energy of 40 kJ/mol (Table

4). These results suggest that O_2 adsorption was largely associative under our experimental conditions.

With the assumption of similar O_2 and H_2 reactions over our catalysts compared to those of Naito and Tanimoto, the following explanation can be proposed for our adsorption calorimetry results. Initially, O_2 adsorbs associatively (reaction 1 in Table 5), and only strongly bound species on small gold particles remain after evacuation. On H_2 introduction, adsorbed oxygen facilitates H_2 dissociation through the formation of OOH species (reaction 8 in Table 5). These hydrogen peroxy species, as discussed in the section on the DFT results, are likely to decompose on small gold particles by splitting off H (the reverse of reaction 3 in Table 5), and therefore, the overall reaction is dissociative hydrogen adsorption (reaction 2 in Table 5). We emphasize that dissociative hydrogen adsorption, reaction 2 in Table 5, is not an elementary step in our mechanism and that this presentation of a series of steps as a single adsorption reaction was done in order to simplify the definition of kinetic model parameters and derivation of rate expressions. The calculated energy changes for dissociative hydrogen adsorption of -163 kJ/mol for Au_5 and -116 kJ/mol for Au_{13} are consistent with the heat evolution of -120 to -150 kJ/mol in H_2 back-titration experiments. A rapid decline in the heat evolution and subsequent apparent saturation observed experimentally on additional H_2 introduction can be attributed to a reduction in the heat of adsorption with coverage and eventual saturation of the small Au particles, where the strongly bound O_2 was initially adsorbed. An alternative explanation to account for the H_2/O_2 surface coverage ratios in Table 1 based on the formation of OH, H_2O_2, or H_2O surface species would be inconsistent with the DFT estimates for the stability of these species on small gold particles.

Benton and Elgin conducted experiments with solid gold in 1927 and reported apparent reaction orders of 1 in P_{H_2} and 0.5 in P_{O_2}, close to our values summarized in Table 4.[2] Our values are also similar to the orders of 1 in P_{H_2} and 0 in P_{O_2} reported by Bone and Wheeler for a gold gauze in 1906.[1]

Our kinetic results in Figures 10 and 11 show that there was no significant difference in water formation rates for catalysts with the Si−MFI and Ti−MFI supports. This suggests that proximity of Au particles to Ti sites in the MFI structure either reduces or does not change significantly the reactivity of Au toward H_2O formation. Specifically, if random nucleation of Au particles is assumed (1), the number of Au sites in proximity to Ti would be on the order of 1 in 70. So if the reactivity of Au particles close to Ti were lower than or substantially similar to that of Au particles associated with silica only, then this would not detectably affect the overall rate. If preferential location of Au particles in proximity to Ti sites is assumed (2), then the activity of Au particles was largely unaffected by the Au−Ti interface. It was possible for each Au particle to be in proximity of a Ti site because the catalyst had a Ti/Au ratio of 27. The absence of evidence for the effect of the gold−support interactions on the reaction rate confirms our initial assumption that the gold particle size is the major effect in determining the catalyst activity, and, accordingly, only this effect is considered in the following development and discussion of the reaction mechanism.

In the development of a reaction mechanism for a description of our kinetic measurements, we constrained the selection of possible reactions based on our catalyst characterization and computational results. In addition, the selection of the major reaction pathways and mechanism simplifications were made based on the studies of Naito and Tanimoto[9] and literature data

for O_2 and H_2 adsorption. We first consider results for O_2 adsorption (reaction 1 in Table 5). The activation energy for O_2 adsorption on a gold wire at $323-673$ K was estimated to be 13 kJ/mol by Kul'kova and Levchenko.[28] A similar value of 12 kJ/mol was estimated by Choi et al. for 5 wt % Au/SiO_2.[29] A higher estimate of 26 kJ/mol was obtained by Kislyuk and Tret'yakov using a gold filament at $1100-1200$ K.[27] A comparison of these values with our apparent activation energy of 40 kJ/mol (Table 4) suggests that associative O_2 adsorption under our conditions should be fast. This step, therefore, can be treated as being quasi-equilibrated for all gold particles with the exception of very small ones where O_2 binds strongly. Similarly, oxygen-assisted dissociation of hydrogen can be expected to be a facile step based on the calculated barrier of 10 kJ/mol (reaction 3 in Table 6). Therefore, dissociative hydrogen adsorption can also be treated as a potentially equilibrated step (reaction 2 in Table 5), depending on the heat of H_2 adsorption. Furthermore, the OOH formation step (reaction 4 in Table 6 and reaction 3 in Table 5) is predicted to have a small barrier of 22 kJ/mol, and this step can also be equilibrated. On the basis of the energy diagram in Figure 6, the rate-determining step is likely to be the reaction between surface OOH species and gas-phase hydrogen (reaction 1 in Table 6 and reaction 4 in Table 5). On the basis of the Au(211) transition state calculations (Figures 6b and 8b), the subsequent decomposition of H_2O_2 intermediate is likely to be fast and irreversible (reactions 5 in Table 5). This mechanism leads to the following rate expression (eq 1):

$$r_{H_2O} = \frac{kK_{OOH}K_{O_2}P_{O_2}\sqrt{K_{H_2}P_{H_2}}P_{H_2}}{(1 + \sqrt{K_{H_2}P_{H_2}} + K_{O_2}P_{O_2} + K_{OOH}K_{O_2}P_{O_2}\sqrt{K_{H_2}P_{H_2}})^2}$$

(1)

where k is the rate constant for the rate-determining step, and K values are equilibrium constant for O_2 adsorption, H_2 adsorption and OOH formation. However, this rate expression is inconsistent with experimentally observed slightly positive apparent oxygen reaction orders and with fractional hydrogen orders of about 0.8 (Table 4). Furthermore, even if some other subsequent step (reactions 5−7 in Table 5) were assumed to be rate determining instead of H_2O_2 formation (reaction 4 in Table 5), the rate expression (eq 1) would be modified with additional terms but would still maintain the same form that is inconsistent with the experimental fractional reaction orders.

In addition to the oxygen-assisted hydrogen dissociation, an autocatalytic mechanism was considered. In this mechanism, OOH and OH intermediates are produced in a reaction between adsorbed O_2 and H_2O (reaction 11 in Table 5). The DFT calculations suggest that this reaction is feasible. However, such a mechanism would predict a dependence of the reaction rate on the H_2O concentration, which was not observed experimentally (Figure 12).

An inconsistency between the apparent reaction orders predicted by the rate expression (eq 1) and experimental values arises from the fact that the denominator of the equation is squared, i.e., from the assumption in the mechanism that two identical surface sites are involved in the rate-determining step (for reaction 4 in Table 5, one site is occupied by OOH and the second one is vacant). One possible modification of the reaction mechanism, which will make the rate expression consistent with the experimental data, is to assume that only a single surface site is involved in the rate-determining step. For example, H_2O_2 can be assumed to form in a single step between adsorbed O_2 and gas-phase H_2. A computational evaluation of this reaction

TABLE 7: Reaction Mechanism Based on a Two-site Model and Kinetic Model Parameters[a]

reaction	ΔG fitted, kJ/mol
1. O_2(gas) + * $\rightleftarrows$ O_2*	−29.8
2. H_2 (gas) + 2* $\rightleftarrows$ 2H*	−40.0
H_2 (gas) + 2□ $\rightleftarrows$ 2H□	
3. O_2* + H□ $\rightleftarrows$ OOH* + □	16.4

reaction	E_a fitted, kJ/mol
4. OOH* + H_2 (gas) + □ → H_2O_2* + H□ (RDS)	24.0[b]

	ratio of active sites
5 wt % Au on SiO_2	2.5×10^{-3}
0.15 wt % Au on SiO_2	1.5×10^{-2}
0.15 wt % Au on Si−MFI	1.0
0.15 wt % Au on Ti−MFI	0.9
0.15 wt % Au on Si−MFI after high T treatment	1.0

[a] See key for Table 6. [b] With preexponential fixed at 10^5 Pa/s.

with the Au(211) model suggests that it is unlikely to be an elementary step as there are multiple bonds being formed and broken at the same time. In addition, transition state calculations for reactions involving gas-phase H_2 (reactions 1 and 3 in Table 6) indicate that prior to reaction, H_2 can be stabilized, even if only weakly, by the surface, and that the splitting of a hydrogen molecule is facilitated by stabilization of one of its atoms by the surface. As a result, an additional surface site appears to be required for H_2O_2 formation. Another possible modification of the mechanism that can be made in order to change the rate expression is to assume that an additional surface site is not identical to the first one. Our calculations with Au(211) appear to support such an assumption, i.e., that there is one type of sites where O_2, OOH, and H compete for adsorption and another type of sites where O_2 and OOH adsorb so weakly that they do not interfere with H adsorption. A modified two-site adsorption mechanism is presented in Table 7. For simplicity, the energetics of hydrogen adsorption on two types of sites were not distinguished. This mechanism yields the following rate expression:

$$r_{H_2O} =$$

$$\frac{kK_{OOH}K_{O_2}P_{O_2}\sqrt{K_{H_2}P_{H_2}}P_{H_2}}{(1 + \sqrt{K_{H_2}P_{H_2}} + K_{O_2}P_{O_2} + K_{OOH}K_{O_2}P_{O_2}\sqrt{K_{H_2}P_{H_2}})(1 + \sqrt{K_{H_2}P_{H_2}})}$$

(2)

This rate expression (eq 2) based on the dual-site adsorption model was fitted to the experimental data by adjusting ΔG values for O_2 and H_2 adsorption, and for OOH formation (reactions 1−3 in Table 7), which define, correspondingly, K_{O_2}, K_{H_2}, and K_{OOH}. The reaction rate constant for H_2O_2 formation (reaction 4 in Table 7) was fitted as a product of a preexponential factor and an activation energy term, $k = A \exp(-E_a/RT)$. As the apparent activation energy should be close to the experimental values of 37−41 kJ/mol (Table 4), the value of the preexponential factor could be estimated. It was found to be on the order of 10^5 (Pa s)$^{-1}$ for the reaction rate expressed as turn over frequencies (TOF) based on the total number of Au atoms. The value of A was fixed at 10^5 (Pa s)$^{-1}$ and subsequently not varied with other model parameters. The similarity between the apparent reaction orders and activation energies for the tested catalysts in Table 4 suggests that there is a common reaction mechanism and that the differences in activity are due mainly to the differences in the concentration of active sites. Accordingly, the kinetic data for all catalysts were fitted simultaneously

with the same rate expression (eq 2) with an adjustment for the concentration of active sites for each catalyst. The adjustment was made with multiplication factors, which were calculated as a ratio of the activity for a particular catalyst to the activity of the most active catalyst, 0.15 wt % Au/Si−MFI, at the base kinetic conditions. If we assume that all Au atoms were active for H_2O formation on the 0.15 wt % Au/Si−MFI (multiplication factor of unity), then the multiplication factors for other catalysts would signify the ratio of active Au atoms. The calculated ratios of active Au sites used in the model fit are shown in Table 7.

Large gold particles (larger than Au_{55}) can be expected to be catalytically inactive because of their inability to adsorb oxygen. On the other hand, small gold particles (Au_5 and smaller) are also likely to be inactive for water production because the formation of OOH and H_2O_2 intermediates is estimated to be energetically unfavorable on such surfaces (reactions 3 and 12 in Table 5 and Figure 7). Therefore, only intermediate-size gold particles (on the order of $Au_{13}-Au_{55}$) are likely to determine the catalytic activity, and, consequently, the reaction energy estimates for Au_{13} and Au_{55} (ΔE values for reactions 1−3 in Table 5) were used as initial guesses for the fitted model parameters (ΔG values in Table 7). With both initial parameter sets, a starting value of 32 kJ/mol was used to fit the activation energy based on the transition state calculations with the Au(211) model (reaction 1 in Table 6). Fitting ΔG and E_a values with the Au_{13} and Au_{55} initial estimates converged to the same optimized parameter values shown in Table 7. The fitted ΔG value for oxygen adsorption of −29.8 kJ/mol is close to the initial estimate of −53 kJ/mol for Au_{13}. Weaker adsorption is in line with the high coverage calculations on Au(211) (Figure 7), which suggest that oxygen on the surface destabilizes by about 25 kJ/mol due to the presence of neighboring species. The fitted ΔG value for hydrogen adsorption of −40 kJ/mol is higher than the initial estimate for Au_{13} by 76 kJ/mol. This significant difference is mainly due to the fact that the estimate was obtained for the preferential hydrogen adsorption site on a clean surface, whereas the model value describes adsorption on alternative adsorption sites when the preferential site is occupied by an oxygen-containing species. As mentioned above, the difference in binding energies on the two types of sites on Au(211) for a hydrogen atom was calculated to be 27 kJ/mol, which yields the difference of 54 kJ/mol for the adsorption of H_2. The fitted ΔG value for the formation of OOH species of 16.4 kJ/mol is similar to the initial estimate of 1 kJ/mol for Au_{13} (reaction 3 in Table 5). The fact that the fitted ΔG values are comparable to the apparent experimental activation energy of about 40 kJ/mol is consistent with the model assumption that reactions 1−3 in Table 7 are equilibrated. If these reactions were significantly exothermic or endothermic, they would be effectively irreversible. The similarity of the fitted values to the estimates for Au_{13} confirms the initial assumption that intermediate-size gold particles are most active catalytic sites for water production. This dependence of the catalytic activity on the size of gold particles provides guidance on the reasons for the observed difference in the reaction rates between the catalysts with the amorphous SiO_2 and MFI supports. Specifically, it is likely that most gold atoms on the MFI supports are located inside the pores. The gold particles inside the pores are limited in size to be on the order of Au_{13}, which would be most reactive for water formation. The number of these intermediate-size gold particles with the size of ∼7 Å was not estimated by TEM for catalysts with the amorphous support (Figure 4a) because of the detection limit, but it is likely that their relative ratio was lower. Therefore, the difference in reaction rates

Water Synthesis over Gold Nanoparticles

J. Phys. Chem. B, Vol. 109, No. 6, 2005 **2273**

between the amorphous SiO_2 and MFI supports can be attributed to the difference in the number of gold particles that are similar in size to Au_{13}.

The fitted parameters accurately describe the experimental data, as can be seen in Figures 10 and 11 where the calculated rates are presented graphically as lines. A comparison of the apparent reaction orders and the activation energy for the fitted model and the experimental values in Table 4 shows that they match closely. This agreement can be understood by analyzing the relative significance of individual terms in the rate eq 2. The term for the hydrogen surface coverage, $\sqrt{K_{H_2}P_{H_2}}$, is larger than unity, and the $(1 + \sqrt{K_{H_2}P_{H_2}})$ expression in the denominator essentially cancels the $\sqrt{K_{H_2}P_{H_2}}$ term in the numerator. This is the cancellation of the requirement of a surface H for OOH formation (reaction 3 in Table 7) and of a vacant site for hydrogen adsorption in H_2O_2 formation (reaction 4 in Table 7). If the term for the O_2 surface coverage, $K_{O_2}P_{O_2}$, were so large as to completely dominate the first bracketed expression in the denominator, it would cancel out the same term in the numerator and a zero order in oxygen and first order in hydrogen would be predicted. Instead, model values for the $K_{O_2}P_{O_2}$ term are large but comparable to the values for the OOH coverage term and, therefore, an order in oxygen of slightly above zero and an order in hydrogen below unity are predicted, in agreement with the experimental results. This kinetic model, thus, predicts that the most abundant surface species on the active Au sites would be O_2 and OOH with some addition of H. The OOH species have recently been observed with inelastic neutron scattering by Goodman et al. for the reaction of O_2 and H_2 over Au/TiO_2.[30] With respect to the OH groups, the model assumes that once they are formed on H_2O_2 decomposition, they quickly and irreversibly react with surface H to make water. Therefore, the concentration of OH groups is likely to be small, and it should not influence the reaction rate. With respect to the model prediction for the apparent activation energy, the value is composed essentially as the sum of ΔG for OOH formation and the intrinsic activation energy for the H_2O_2 formation step (Table 7), $16.4 + 24.0 = 40.4$ kJ/mol, since the effect of the $K_{O_2}P_{O_2}$ term in the numerator is small because of the cancellation with the denominator.

In summary, our results suggest that the mechanism of water formation over gold proceeds through the formation of an OOH intermediate. On small gold particles, where O_2 adsorbs strongly, this hydrogen peroxide intermediate is likely to decompose to surface O_2 and H. On such small particles, the rate of H_2O formation is expected to be minimal, and the main reaction is predicted to be oxygen-assisted hydrogen dissociation. On large gold particles, which do not adsorb O_2 under our reaction conditions, oxygen and hydrogen are expected to be mostly unreactive. On intermediate-size gold particles, comparable in size to Au_{13}, where O_2 adsorbs weakly, the hydrogen peroxide intermediate can react with additional hydrogen to form H_2O_2, which then decomposes to OH groups that react further with hydrogen to produce water.

5. Conclusions

The reaction mechanism of water formation from H_2 and O_2 was studied over a series of silica-supported gold nanoparticles (Table 1). The metal particle size distributions were estimated with TEM and XRD measurements. Hydrogen and oxygen adsorption calorimetry was used to probe the nature and properties of surface species formed by these molecules. DFT calculations with model surfaces were performed to estimate

the thermodynamic stability and reactivity of surface species. Kinetic data on the partial pressure dependences and the activation energy were collected with and without water in the inlet stream.

1. Calorimetry measurements were performed for O_2 adsorption and subsequent H_2 back-titration at 400 K. The initial heat of O_2 adsorption was -150 to -220 kJ/mol. The total coverage of strongly bound oxygen associated with heat evolution was $2-3\%$ of the total number of Au atoms for the 0.15 wt % Au catalysts and 0.2% for the 5 wt % Au catalyst. The amount of strongly bound oxygen did not correlate with the catalyst activity toward water formation. The initial heat of H_2 adsorption during the back-titration was -120 to -150 kJ/mol. The saturation H_2 coverage corresponded to the H_2O stoichiometry based on the coverage of the strongly bound oxygen.

2. DFT calculations were performed with Au_5, Au_{13}, and Au_{55} clusters and with Au(111) and Au(211) periodic slabs. Adsorption energies for various surface species were estimated with these models (Table 2). In general, surface species were found to be more stable on small Au particles. The calculations predicted that the stability of O_2, OOH, and OH surface species was most sensitive to the size of Au particles. The adsorption energies of H_2, H_2O, and H_2O_2, in contrast, were found to be small (within -30 kJ/mol) and practically structure insensitive.

3. Apparent partial pressure dependences and activation energies were similar for all catalysts (Table 4). The apparent power-law reaction orders in H_2 pressure for $0.5-20$ kPa at 2.5 kPa of O_2 at 433 K were all below unity: $0.7-0.8$. The apparent orders in O_2 pressure for $2-40$ kPa at 5 kPa of H_2 at 433 K were close to zero: $0.1-0.2$. The apparent activation energies were $37-41$ kJ/mol at 2.5 kPa of O_2 and 5 kPa of H_2 and $383-483$ K. The 5 wt % Au/SiO_2 sample exhibited the lowest absolute activity based on the total number of Au atoms. The activity of the 0.15 wt % Au/SiO_2 sample was 6 times higher; and the activities of the MFI-supported samples were all similar and significantly, $360-400$ times, higher.

4. All kinetic measurements were repeated with 3 vol % H_2O in the inlet stream. Within the experimental accuracy, the H_2O addition did not change the catalyst activities, apparent activation energies or reactant orders.

5. Catalysts with 0.15 wt % Au on Si$-$MFI (Silicalite-1) and Ti$-$MFI (TS-1 with 1 wt % Ti) exhibited similar activities.

6. The mechanism of water formation over gold is proposed to proceed through an OOH intermediate. This hydrogen peroxide intermediate can react with hydrogen to form H_2O_2, which then decomposes to OH groups that react further with additional hydrogen (Table 6). A rate expression derived based on this mechanism (eq 2) accurately describes the experimental kinetic data.

7. The higher activity of the MFI-supported catalysts is attributed to a higher concentration of gold particles comparable in size to Au_{13}, which can fit inside MFI pores. DFT results suggest that such intermediate-size gold particles are most reactive toward water formation. Smaller particles are proposed to be less reactive due to the instability of the OOH intermediate, whereas larger particles are less reactive due to the instability of adsorbed oxygen.

References and Notes

(1) Bone, A. W.; Wheeler, R. V. *Philos. Trans.* **1906**, *206A*, 1.

(2) Benton, A. F.; Elgin, J. C. *J. Am. Chem. Soc.* **1927**, *49*, 2426.

(3) Ostrovskii, V. E.; Dobrovol'skii, N. N. *Proc. Int. Congr. Catal., 4th* **1971**, *2*, 9.

(4) Jones, C. A.; Grey, R. A. US 6,468,496, A1, 2002.

(5) Landon, P.; Collier, P. J.; Papworth, A. J.; Kiely, C. J.; Hutchings, G. J. *Chem. Commun. (Cambridge. U.K.)* **2002**, 2058.

(6) Okumura, M.; Kitagawa, Y.; Yamagcuhi, K.; Akita, T.; Tsubota, S.; Haruta, M. *Chem. Lett.* **2003**, *32*, 822.

(7) Suh, M.; Bagus, P. S.; Pak, S.; Rosynek, M. P.; Lunsford, J. H. *J. Phys. Chem. B* **2000**, *104*, 2736.

(8) Cho, A. *Science* **2003**, *299*, 1684.

(9) Naito, S.; Tanimoto, M. *J. Chem. Soc., Chem. Commun.* **1988**, 832.

(10) Taramasso, M.; Perego, G.; Notari, B. US 4,410,501, A1, 1983.

(11) Lopez, N.; Janssens, T. V. W.; Clausen, B. S.; Xu, Y.; Mavrikakis, M.; Bligaard, T.; Norskov, J. K. *J. Catal.* **2004**, *223*, 232.

(12) Shen, J.; Hill, J. M.; Watwe, R. M.; Podkolzin, S. G.; Dumesic, J. A. *Catal. Lett.* **1999**, *60*, 1.

(13) O'Rear, D. J.; Loeffler, D. G.; Boudart, M. *J. Catal.* **1990**, *121*, 131.

(14) Benson, J. E.; Hwang, H. S.; Boudart, M. *J. Catal.* **1973**, *30*, 146.

(15) Benson, J. E.; Boudart, M. *J. Catal.* **1965**, *4*, 704.

(16) Berndt, H.; Pitsch, I.; Evert, S.; Struve, K.; Pohl, M.-M.; Radnik, J.; Martin, A. *Appl. Catal., A: Gen.* **2003**, *244*, 169.

(17) Mills, G.; Gordon, M. S.; Metiu, H. *J. Chem. Phys.* **2003**, *118*, 4198.

(18) Bonacic-Koutecky, V.; Burda, J.; Mitric, R.; Ge, M.; Zampella, G.; Fantucci, P. *J. Chem. Phys.* **2002**, *117*, 3120.

(19) Oviedo, J.; Palmer, R. E. *J. Chem. Phys.* **2002**, *117*, 9548.

(20) Mavrikakis, M.; Stoltze, P.; Norskov, J. K. *Catal. Lett.* **2000**, *64*, 101.

(21) Liu, Z.-P.; Hu, P.; Alavi, A. *J. Am. Chem. Soc.* **2002**, *124*, 14770.

(22) Trapnell, B. M. W. *Proc. R. Soc. (London)* **1953**, *A218*, 566.

(23) Pritchard, J.; Tompkins, F. C. *Trans. Faraday Soc.* **1960**, *56*, 540.

(24) Wells, D. H.; Delgass, W. N.; Thomson, K. T. *J. Catal.* **2004**, *225*, 69.

(25) Paredes Olivera, P.; Patrito, E. M.; Sellers, H. *Surf. Sci.* **1994**, *313*, 25.

(26) Chesters, M. A.; Somorjai, G. A. *Surf. Sci.* **1975**, *52*, 21.

(27) Kislyuk, M. U.; Tret'yakov, I. I. *Kinet. Katal.* **1979**, *20*, 925.

(28) Kul'kova, N. V.; Levchenko, L. P. *Kinet. Katal.* **1965**, *6*, 765.

(29) Choi, K.-H.; Coh, B.-Y.; Lee, H.-I. *Catal. Today* **1998**, *44*, 205.

(30) Sivadinarayana, C.; Choudhary, T. V.; Daemen, L. L.; Eckert, J.; Goodman, D. W. *J. Am. Chem. Soc.* **2004**, *126*, 38.